

MIT Open Access Articles

*Electrochemical Fluoridation of Manganese Oxide by
Perfluorinated Gas Conversion for Lithium Ion Cathodes*

The MIT Faculty has made this article openly available. **Please share**
how this access benefits you. Your story matters.

Citation: H. Gao, M. He, R. Guo, B. M. Gallant, Batteries & Supercaps 2021, 4, 1771.

As Published: <http://dx.doi.org/10.1002/batt.202100139>

Publisher: Wiley

Persistent URL: <https://hdl.handle.net/1721.1/140407>

Version: Author's final manuscript: final author's manuscript post peer review, without publisher's formatting or copy editing

Terms of use: Creative Commons Attribution-Noncommercial-Share Alike



Author Manuscript

Title: Electrochemical Fluoridation of Manganese Oxide by Perfluorinated-Gas Conversion for Li-ion Cathodes

Authors: Haining Gao; Mingfu He; Rui Guo; Betar M. Gallant

This is the author manuscript accepted for publication. It has not been through the copyediting, typesetting, pagination and proofreading process, which may lead to differences between this version and the Version of Record.

To be cited as: 10.1002/batt.202100139

Link to VoR: <https://doi.org/10.1002/batt.202100139>

Electrochemical Fluoridation of Manganese Oxide by Perfluorinated-Gas Conversion for Li-ion Cathodes

Haining Gao, Mingfu He, Rui Guo and Betar M. Gallant*

H. Gao

Department of Materials Science and Engineering, Massachusetts Institute of Technology, 77 Massachusetts Avenue, Cambridge, Massachusetts 02139, United States

Dr. M. He, R. Guo, Prof. B. M. Gallant

Department of Mechanical Engineering, Massachusetts Institute of Technology, 77 Massachusetts Avenue, Cambridge, Massachusetts 02139, United States

E-mail: bgallant@mit.edu

Abstract: Fluoridation of Li-ion cathodes is of growing interest for high-capacity Li^+ storage materials, but well-controlled fluoridation processes are elusive. We investigated an electrochemical methodology to grow lithium fluoride (LiF) by reduction of perfluorinated gas onto metal oxides (MO), which then forms M-O-F by splitting of lithium fluoride (LiF) upon charge, using MnO as an example target phase. Unlike current methods where particle size <10 nm is necessary for high MnO utilization (subsequent discharge/lithiation capacity), owing to the nano-crystallinity and intimate contact of electrochemically-grown LiF, high MnO utilization (~ 0.9 e $^-$ /MnO, 340 mAh g $_{\text{MnO}}^{-1}$) is achieved with large MnO particle size (~ 400 nm), exceeding comparable MnO/LiF systems reported to date. Additionally, incorporation of perfluorinated-gas additive benefits cycling, with capacity of ~ 270 mAh g $_{\text{MnO}}^{-1}$ retained after 20 cycles. This work demonstrates the opportunity for electrochemically-driven fluoridation to achieve high capacities with larger particle sizes needed to bring oxyfluorides closer to practical reality.

1. Introduction

Sustained demand for higher-energy rechargeable Li/Li-ion batteries that can reach U.S. Department of Energy targets of 500 Wh/kg and 1000 Wh/L motivates continued improvement beyond today's cathode materials, which limit cell performance.^[1] Commercialized Li-ion battery cathodes belong mainly to oxide-

based materials, with current focus on lithium nickel-manganese-cobalt oxide (NMC) with capacities of ~ 200 mAh g⁻¹.^[2] Many oxides currently under development that can attain higher capacities, such as Li-rich cathodes (*e.g.* Li-rich NMC, >280 mAh g⁻¹)^[3] or Li-rich disordered rock-salt phases (>300 mAh g⁻¹),^[4] rely on anionic redox, which triggers oxygen release along with transition metal dissolution during cycling, plaguing cell stability.^[5] In this context, there has been great interest in identifying strategies to improve cyclability of oxide parent phases, of which fluorination/fluoridation methods have received focus in recent years.^[6] The high electronegativity of fluorine (F) and exceptionally high free energy of formation of fluorides imparts strong metal–F bonds,^[7] stabilizing transition metal species from migration and improving lattice stability. Bulk-phase F-substitution for oxygen (O) has so far been conducted in oxides with various structures (spinel LiMn₂O₄, layered NMC, and Nb-based disordered rock-salt), yielding improved cyclability, higher discharge voltage, and increased capacity.^[6b-f, 8] In addition to bulk substitution, surface F-modification, such as nanoscopic LiF coatings, can protect the oxides against the electrolyte under highly oxidizing conditions, helping to suppress side reactions while sustaining prolonged cycle life.^[6g]

More recently, LiF surface modification has been reported to support bulk-like fluoridation of oxide phases upon electrochemical activation at high potentials. Kang and co-workers, using composites composed of LiF and non-lithiated transition metal oxides synthesized by high energy ball milling, demonstrated that the initial charge step induces an LiF “splitting” (activation) reaction upon oxidation of a nearby transition metal site, *viz.*: $MO + LiF \leftrightarrow MOF + Li^+ + e^-$ ($M = Mn, Fe, \text{ or } Co$).^[9] When used with a non-Li-containing oxide like the monoxide class MO, LiF acts as both an F and a Li source, with Li⁺ migration to the anode as F is incorporated into the cathode to balance oxidation of M, and thus has an additional benefit of providing Li to the cathode and cell. Following activation, the resulting M–O–F phase, which reportedly has a disordered structure with an F-rich amorphous shell and an O-rich core, then cycles as a conversion cathode with reversible capacities up to 240 mAh g_{MnO+LiF}⁻¹ (or ~ 345 mAh g_{MnO}⁻¹). Achieving these capacities previously required very small oxide/LiF particle sizes (< 10 nm for MO), which were reported as necessary

to achieve meaningful degrees of fluoridation. This occurs because, upon first charge, F largely concentrates in the MnO surface region; consequently, large surface areas are needed to facilitate high MnO utilization.^{[9b,}

^{10]} In contrast to mechanical milling, Tarascon and co-workers proposed a distinct approach for *in situ* fluoridation of oxides through LiPF₆ salt decomposition, attaining a capacity of ~250 mAh g_{MnO}⁻¹.^[11] However, the decomposition of salt demands excess electrolyte and will inevitably lead to other parasitic reactions. Finally, thin-film methods, such as pulse laser deposition (PLD), have recently been explored to form LiF/Fe/Cu or LiF/NiFe₂O₄ films with small domain sizes for both LiF and M/MO phases (< 10 nm) and improved contact between LiF and transition metal species.^[12] Scalability of the thin film processing methods requires further development. Consequently, methodologies of F incorporation need further exploration and improvement to broaden applicability to practical battery materials, especially where high tap densities require larger particle sizes (up to ~several μm)^[13] and where parasitic salt consumption is untenable.

We hypothesized, given extensive reliance on ball-milling in previous work and known difficulty in LiF processing to form well-controlled interfaces, that poor physical/electrical contact between the MO substrate and LiF could limit attainable degrees of fluoridation below what may be achievable, contributing to stringent particle-size requirements seen previously. To test this hypothesis, and to examine another possible fluoridation methodology with potential to help elucidate the limitations of those used so far, this study investigated whether higher degrees of fluoridation, as evidenced by higher discharge capacities, are achievable using an electrochemically-sourced LiF formed by reduction of perfluorinated gases. Recently, we have found that the full reduction of SF₆ ($\text{SF}_6 + 8\text{e}^- + 8\text{Li}^+ \rightarrow \text{Li}_2\text{S} + 6\text{LiF}$)^[14] and NF₃ ($\text{NF}_3 + 3\text{e}^- + 3\text{Li}^+ \rightarrow 3\text{LiF} + \frac{1}{2}\text{N}_2$)^[15] occurs on carbon cathodes at potentials of ~2-3 V vs. Li/Li⁺, thus the gases act as a highly-F-dense and electroactive molecular LiF source. Moreover, the morphology of the electrochemically-formed LiF, which nucleates and grows as nanoscale particles (with diameters ranging from 20 nm to >400 nm) on the cathode substrate, was found to be highly versatile and could be tailored by modulating conditions such as electrolyte, discharge rate, and capacity. Herein, we examine the electrochemical nucleation and growth

of LiF from these perfluorinated gases to form an intimate coating on an electronically-conductive oxide for the first time (**Figure 1**). Owing to the good contact with MnO and the nano-crystallinity of LiF, we find that the electrochemically-formed, LiF-coated MnO exhibits higher utilization ($\sim 0.9 \text{ e}^-/\text{MnO}$) with larger particles ($\sim 400 \text{ nm}$), consistent with a higher degree of fluorination, compared to the ball-milled composites ($\sim 40 \text{ nm}$, $< 0.7 \text{ e}^-/\text{MnO}$) and those fluorinated from salt-based reactions previously reported with similar particle sizes ($\sim 0.6 \text{ e}^-/\text{MnO}$).^[11]

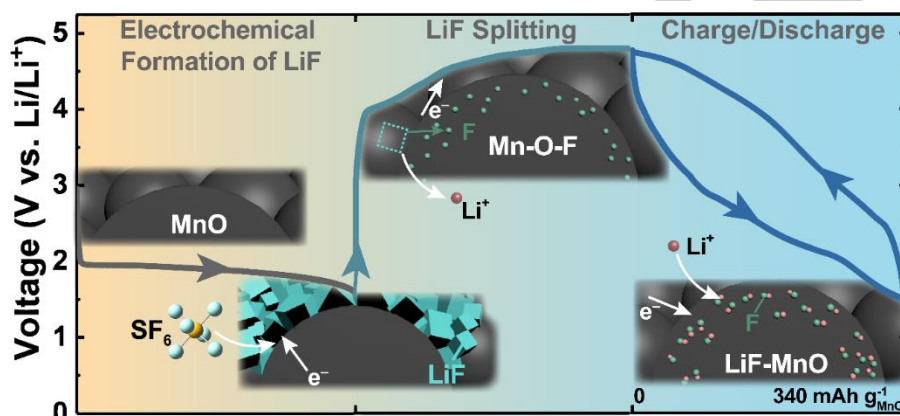


Figure 1. Schematic depicting electrochemical fluorination of MnO cathodes using SF_6 gas as an exemplar fluorination source. Step 1: Electrochemical nucleation and growth of LiF occurs on MnO upon cathodic SF_6 reduction. Step 2: MnO/LiF electrodes are charged to induce electrochemical splitting of LiF and concurrent MnO fluorination; as depicted, this process initiates at the surface of MnO particles and can continue into the bulk as charging proceeds. Step 3: Subsequent cycling occurs between the nominal end phases $\text{Mn-O-F} \leftrightarrow \text{LiF-MnO}$.

2. Results and discussions

2.1 Electrochemical formation and characterization of LiF coating on MnO

MnO was chosen as a model substrate for fluorination in this work because it has been used in prior LiF splitting studies,^[9b, 11] providing sufficient data for comparison across methodologies, whereas few reports have investigated pre-lithiated Mn-containing compounds. The understanding gained from this study is expected to help with developing fluorinated practical oxide cathodes both without and with intrinsic Li sites. Due to the large particle size of the as-received MnO ($\sim 0.25 \text{ mm}$), a short ball-mill of 3 h was conducted on MnO/Vulcan carbon (VC, $\sim 50 \text{ nm}$) mixture (MnO:VC=7:2 w/w) to reduce the particle size to $\sim 400 \pm 300$

nm (**Figure S1**). The resulting powder was then mixed with VC and polyvinylidene fluoride (PVDF) binder to form cathode materials (with a weight ratio of MnO:VC:PVDF = 55:35:10) and was coated onto Toray paper (5 wt% Teflon treated). In this work, 0.1 M lithium perchlorate (LiClO_4) was used as the salt to eliminate additional F sources in the electrolyte other than the fluorinated gas. For the first discharge (LiF formation step), tetraethylene glycol dimethyl ether (TEGDME) was used as the solvent given its ability to promote more film-like LiF upon SF_6 reduction (typical LiF particle sizes of ~30 nm with conformal coating on carbon) with better electrical contact with the underlying substrate, as opposed to larger discrete LiF particles (~100 nm) with exposed carbon surfaces as observed with higher-donor-number solvents like DMSO.^[14b] In addition, SF_6 exhibits higher discharge capacity in ethers than in carbonate solvents^[14a] allowing more versatility for tailoring and studying electrochemically-formed LiF on MnO. Swagelok-type cells were assembled with Li anodes, the indicated cathode and electrolyte, and were purged with SF_6 or NF_3 pressurized to ~1 bar (typical gas solubilities ~1-5 mM)^[14a, 15] and sealed for testing.

Typical first-discharge profiles under galvanostatic conditions are shown in **Figure 2a**. Without any fluorinated gas, MnO electrodes exhibited negligible capacity upon discharge (~30 mAh $\text{g}_{\text{MnO}}^{-1}$) as expected for Mn^{2+} which is inactive in this voltage window.^[16] In contrast, cells containing fluorinated gas exhibited electrochemical activity corresponding to gas reduction. The discharge potential of NF_3 -containing cells (~2.1 V) at 75 mA g_C^{-1} (~48 mA $\text{g}_{\text{MnO}}^{-1}$) was similar to that on VC cathodes as measured previously,^[15] indicating that the inclusion of MnO does not significantly affect the reduction behavior of NF_3 . Typical discharge capacities of Li- NF_3 cells on MnO/VC cathodes are 1100 mAh $\text{g}_{\text{MnO}}^{-1}$ (~1700 mAh g_C^{-1}), corresponding to an NF_3 (consumed, assuming 3 e^- transfer per NF_3 molecule) to MnO molar ratio of 1:1. X-ray diffraction (XRD) in **Figure 2b** shows that LiF is the only crystalline phase formed following NF_3 reduction. From scanning electron microscopy (SEM), a LiF layer was observed which covers the composite cathode, including the MnO particles, uniformly (**Figure 2c**).

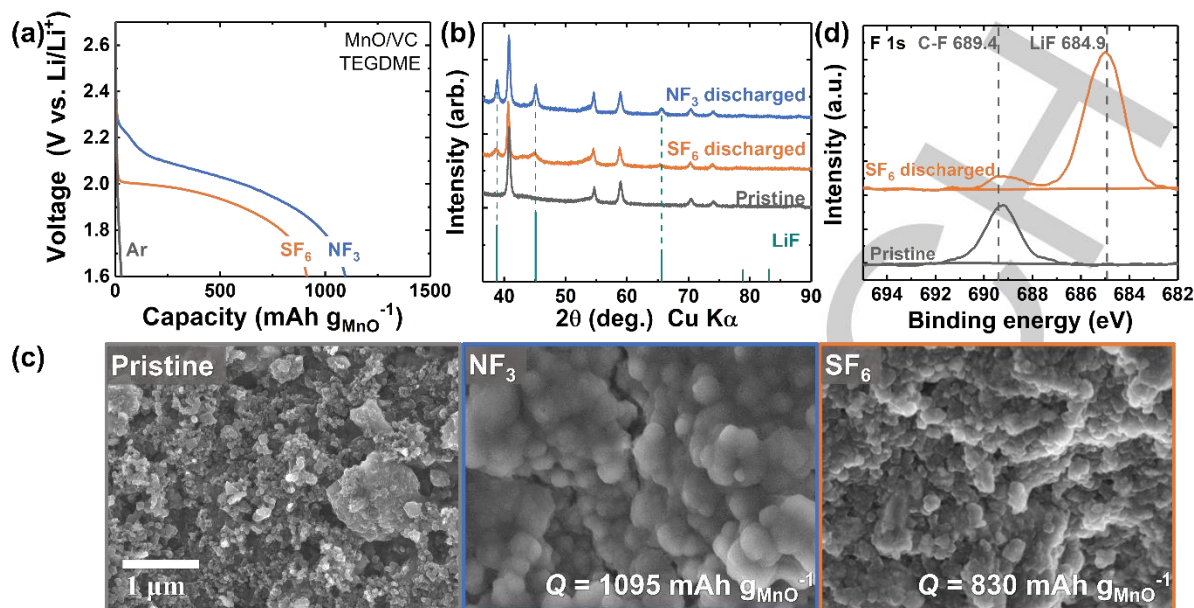


Figure 2. (a) Galvanostatic discharge profiles of Li-SF₆ and Li-NF₃ cells using MnO/VC cathodes as the substrate at 100 mA g_c⁻¹ (~65 mA g_{MnO}⁻¹) and 75 mA g_c⁻¹ (~48 mA g_{MnO}⁻¹), respectively. (b) X-ray diffraction of a discharged electrode in the Li-NF₃ ($Q = 1180 \text{ mAh g}_{\text{MnO}}^{-1}$) and Li-SF₆ ($Q = 830 \text{ mAh g}_{\text{MnO}}^{-1}$) cells. (c) SEM images of pristine electrodes and of electrodes discharged to full capacity using fluorinated gas as indicated. (d) High-resolution F 1s XPS spectra of the discharged electrode of a Li-SF₆ cell. To avoid binder-induced F signal, a non-fluorinated binder, polyacrylonitrile (PAN), was used in the cathode instead of PVDF, thus the capacity (~310 mAh g_{MnO}⁻¹) is lower than in (a) for this particular cell. The C-F peak at 689.4 eV is from Toray paper.

In comparison, discharge of MnO/VC electrodes with SF₆ gas at 100 mA g_c⁻¹ (~65 mA g_{MnO}⁻¹) occurred ~100 mV below NF₃ throughout discharge, which is similar to previous discharge voltages of SF₆ on VC electrodes in TEGDME.^[14b] Typical discharge capacities for SF₆ cells with MnO/VC electrodes are 900 mAh g_{MnO}⁻¹ (~1400 mAh g_c⁻¹), corresponding to a SF₆ (consumed, assuming 8 e⁻ transfer per SF₆ molecule) to MnO molar ratio of 0.3:1. In contrast to reduction of NF₃, only very broad and weak LiF diffraction peaks were detected by XRD after reduction of SF₆ (Figure 2b), which indicates a substantially lower crystallinity and smaller particle sizes for the discharge product. Instead, X-ray photoelectron spectroscopy (XPS) was used to identify the composition of the formed phases. From the F 1s high-resolution scan (Figure 2d), a strong LiF peak at 684.9 eV was observed.^[17] The existence of LiF was further confirmed from liquid ¹⁹F nuclear magnetic resonance (NMR) spectroscopy (Figure S2) upon reacting discharged

cathodes with water (D₂O) to solubilize the LiF, which yielded a strong peak at -122 ppm attributed to LiF.^[18]

A negligible amount of S was detected in the discharged cathode from XPS (**Figure S3**). This is consistent with previous results that showed a tendency of reduced-S phases such as polysulfides to solubilize in the electrolyte upon discharge during SF₆ reduction. Therefore, both cathodes are predominantly LiF-coated MnO with differing degrees of LiF crystallinity. From the SEM image in Figure 2c, the LiF layer formed using SF₆ was similarly uniform and conformal.

2.2 LiF splitting, MnO fluoridation and subsequent lithiation capacity

The MnO activation (charge) process was next investigated using 1 M LiClO₄ in ethylene carbonate and dimethyl carbonate (EC/DMC, v:v = 1:1) as electrolyte, which is more amenable to tolerate the high potentials required upon subsequent charging and LiF splitting when MnO is the substrate. Cells consisted of fresh Li anodes and MnO-containing cathodes, *i.e.* previously-discharged MnO/VC cathodes under NF₃ or SF₆. In these first experiments, the re-assembled cells in carbonate electrolyte contained no fluorinated gas. Except where otherwise noted, the first charge of the MnO, with or without LiF present, consisted of a constant current (CC) process at 20 mA g_{MnO}⁻¹ (~ 0.05 C) to a cutoff of 4.8 V vs. Li/Li⁺, followed by a constant voltage (CV) hold until the current decreased below 10 mA g_{MnO}⁻¹.^[9b, 11a] Henceforth, discharge rates are normalized to the weight of MnO instead of carbon as Mn redox is the major contributor of reversible capacity. The theoretical capacity of Mn-O-F, assuming Mn²⁺/Mn³⁺ redox, is 378 mAh g_{MnO}⁻¹. For MnO/VC without LiF, the charge capacity was limited (101 mAh g_{MnO}⁻¹, **Figure 3a**) and reflected only capacitive-like behavior, likely dominated by the carbon particles (*i.e.* no voltage plateau was observed). During the following discharge, small capacity of <80 mAh g_{MnO}⁻¹ was observed, which is $\sim 2\times$ of that observed before with Ar discharge (Figure 2a) given the larger voltage window ($\sim 2\times$, 4.8 V -1.5 V vs. ~ 3.1 V -1.6 V). This indicates no significant change to the MnO phase, which remained electrochemically inactive.



8

A mechanically ball-milled MnO/LiF composite was prepared for comparison, with an MnO/LiF molar ratio of 1:1.2 with 20% LiF excess, and 20 wt% of VC, comparable to that used previously.^[9b] The average particle size of the obtained MnO/LiF is $\sim 40 \pm 25$ nm as measured from SEM (Figure S1), substantially smaller than that used for electrochemical fluoridation used herein. Given the amount of LiF present in the as-prepared ball-milled cathode, full splitting of LiF would correspond to a capacity of 454 mAh g_{MnO}⁻¹, which is in excess of the theoretical capacity of MnO (378 mAh g_{MnO}⁻¹) owing to excess LiF. Experimentally, an initial charge capacity even higher, at 613 mAh g_{MnO}⁻¹, was observed (**Figure 3b**). Excess charge capacity beyond that used to fluorinate MnO is attributed to a combination of capacitive contributions and possibly to side reactions such as electrolyte oxidation, fluorination, or carbon oxidation.^[19] We note that a capacity higher than the theoretical does not imply full conversion of MnO to MnOF. The following discharge/lithiation of the ball-milled MnO/LiF system exhibits a higher capacity of 259 mAh g_{MnO}⁻¹ than that of pristine MnO/VC without LiF, proving successful activation of MnO to the Mn-O-F phase which then serves as a conversion Li-ion cathode. However, the lower capacity compared to the theoretical (378 mAh g_{MnO}⁻¹) confirms the fact that not all MnO was accessed by fluoridation in this system. The lower capacity than reported elsewhere for ball-milled samples (~ 345 mAh g_{MnO}⁻¹) is attributed to the larger particle size ($\sim 40 \pm 25$ nm) used here, vs. 8 nm in literature, since the fluoridation process is mainly surface-controlled and increased particle size reduces the total active surface area for F incorporation.^[9b, 10]

Electrochemically LiF-coated MnO cathodes (henceforth 'LiF@MnO') formed from SF₆ or NF₃ reduction were next compared. For LiF@MnO formed from fully-discharged Li-NF₃ reduction (**Figure 3c**), a relatively limited charge (LiF splitting) capacity of 490 mAh g_{MnO}⁻¹ was observed despite the large amount of LiF (>1100 mAh g_{MnO}⁻¹ or 1.9x excess), implying not all LiF was electronically or electrochemically accessible for subsequent splitting. As a result, only limited capacity (~ 108 mAh g_{MnO}⁻¹) was delivered during the subsequent discharge/lithiation of Mn-O-F, reflecting a low degree of MnO fluoridation/activation. The insufficient LiF splitting and MnO activation may be attributed to the large particle size of the crystallized

LiF formed. Next, to form similar amount of LiF as that in the ball-milled MnO/LiF system, an SF₆ cell was partially discharged (LiF amount of 454 mAh g_{MnO}⁻¹). The obtained LiF@MnO yielded a similar capacity upon charge/activation (633 mAh g_{MnO}⁻¹) as that for ball-milled MnO/LiF (**Figure 3d**), indicating that the charge capacity is proportional to the total LiF quantity. The subsequent discharge/lithiation capacity of this LiF@MnO from the partially-discharged SF₆ cell was, however, only 137 mAh g_{MnO}⁻¹. We hypothesize that this low lithiation capacity is caused by the low degree of coating of MnO by LiF, recalling that LiF forms both on MnO and on VC (with the latter not contributing to reversible capacity) as was further supported by SEM images (**Figure S4**). Thus, to test this hypothesis, LiF@MnO electrodes were formed with even higher LiF amounts by discharging Li-SF₆ cells to completion. As is shown in Figure 3d, a larger capacity (> 1300 mAh g_{MnO}⁻¹) was attained from the first charge of the higher-LiF-loading LiF@MnO (typical resulting CV hold times were ~40 h). This increased capacity can be attributed to the increased amount of LiF, which, if fully decomposed, can contribute a capacity of ~820 mAh g_{MnO}⁻¹. The LiF@MnO from the fully-discharged SF₆ cell yielded a much higher lithiation capacity of ~340 mAh g_{MnO}⁻¹, equivalent to 0.9 e⁻/MnO, comparable to the highest MnO utilization reported to date.^[9b] Additional evaluation of the electrochemical behavior difference of ball-milled MnO/LiF and LiF@MnO (from SF₆ and NF₃ discharge) is shown *via* differential capacity plots in **Figure S5**. During first charge, the LiF@MnO from the fully or partially discharged Li-SF₆ cells exhibit lower onset potential (~4.0 V) than that of the ball-milled MnO/LiF and NF₃-formed LiF@MnO (~4.2 V), indicating clearly that the former two cathodes are more favorable for LiF splitting. During discharge, LiF@MnO from NF₃ discharge and partial SF₆ discharge exhibited negligible activity. In contrast, the LiF@MnO from full SF₆ discharge and the ball-milled MnO/LiF showed similar profiles with two cathodic peaks, in agreement with that observed in a previous study where two peaks located at 2.5 V and 3.75 V were observed and attributed to Mn redox.^[9b] Therefore, LiF@MnO from fully discharged SF₆ cells was used in all following experiments.

We next investigated the potential dependence of F-incorporation in MnO during the LiF splitting process on first charge in greater detail. LiF@MnO was charged following two additional procedures: CC-CV charge up to 4.7 V, and 4.8 V CC charge without a CV hold. Both charge protocols yielded significantly smaller LiF splitting capacity (~ 300 vs. > 900 mAh g_{MnO}⁻¹ for a CC-CV charge up to 4.8 V), and only limited capacity (~ 100 mAh g_{MnO}⁻¹) upon subsequent discharge (**Figure 4a**), indicating insufficient MnO activation. The results reveal that CV charge at 4.8 V is crucial for the activation of bulk MnO to Mn-O-F. This was further confirmed by examination of the bulk Mn valence state by electron energy loss spectroscopy (EELS), focusing on the two charging protocols up to 4.8 V. In **Figure 4b**, the Mn L-edge showed negligible change after only CC charge, however, inclusion of the CV step at 4.8 V resulted in a Mn L₃ peak shifted to higher energy (from 640.2 eV to 641.3 eV), with a significant decrease in the ratio of L₃/L₂ peak areas, corresponding to oxidization of Mn. Raman spectroscopy was further used to probe the MnO bonding environment change (**Figure 4c**). The vibrational band at 645 cm⁻¹ (stretching A_{1g} modes of Mn-O bonds in MnO₆ octahedra) and low frequencies (< 360 cm⁻¹, skeletal vibrations) belong to Mn₃O₄ instead of MnO,^[20] given that, as was found from previous studies, MnO is easily transformed to Mn₃O₄ due to beam irradiation during Raman measurement.^[21] Consistently, the band located at 645 cm⁻¹ corresponding to the initial MnO phase showed negligible change when CC charged to 4.8 V. In contrast, CV charge resulting in a significant red shift of the Mn-O stretch (to ~ 600 cm⁻¹) along with the appearance of multiple small-intensity bands at lower frequencies, which cannot be assigned to any single manganese oxide phase.^[22] The decreased frequency is reflective of the increased Mn-O bond length,^[23] while the different band positions indicate a more complex Mn bonding environment induced by incorporation of F⁻ ions into the MnO lattice, resulting in more defect sites, and potential lattice distortion due to the Jahn-Teller effect of Mn³⁺.^[6b] These findings are consistent with those observed in previous studies on MnO/LiF, where a defective Mn-O-F spinel-like phase was observed after first charge.^[9b, 11b] Notably, such lattice structure change cannot be

triggered without LiF: for pristine MnO without LiF coating, negligible change in Raman spectra can be observed after being CC-CV charged to 4.8 V (**Figure S6**).

The redox process on the MnO surface was also investigated using XPS. From F 1s XPS (**Figure S7**), the decrease in integrated LiF peak intensity, centered at 684.9 eV, after CV charge is consistent with electrochemical LiF splitting initiation at 4.8 V. The increased contribution from the peak at 686.0 eV, which corresponds to the F⁻ ion bonding with the Mn ion,^[9b] also supports the enhanced depth of LiF splitting and F-incorporation upon CC-CV charge. In addition, Li 1s and Mn 3p, which have closely-located binding energies, were examined to provide a clearer observation of the correlated Li and Mn peak evolution (**Figure 4d**). All spectra are normalized by Mn 3p peak integrated area, except for the uncharged LiF@MnO, in which the Mn signal is strongly blocked by the LiF layer on the surface. After the CC charge, the MnO surface was oxidized to a phase resembling Mn₃O₄ (Mn^{2+/3+}) or Mn₂O₃ (Mn³⁺), and retained its oxidation state after further CV charge, suggesting that Mn₃O₄/Mn₂O₃-like phases precede significant fluoridation. Correspondingly, the Li 1s peak intensity decreased significantly after CV charge, indicating LiF decomposition. Upon subsequent discharge/lithiation, the Li 1s peak recovered and the Mn valence state reverted to be close to Mn²⁺, consistent with reversible redox.

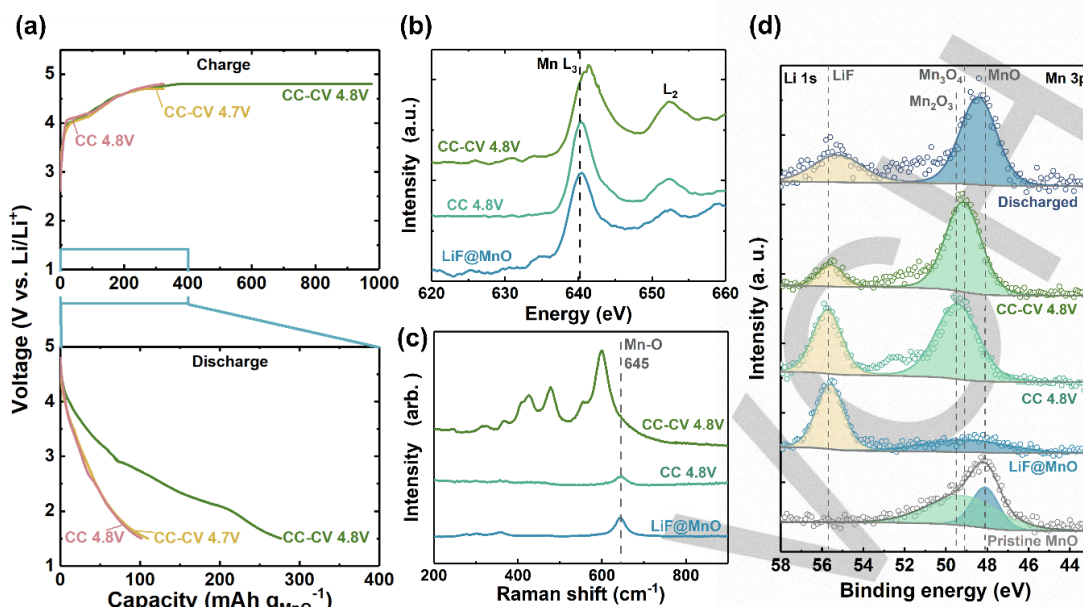


Figure 4. (a) First charge (LiF splitting) and discharge (lithiation) profiles of LiF@MnO (from fully discharged Li-SF₆ cells; also used for part b–d) at 20 mA g_{MnO}⁻¹ with different charge procedures: CC-CV charged to 4.8 V, CC-CV charged to 4.7 V, or CC charged to 4.8 V. Both CV charges were cut off at 10 mA g_{MnO}⁻¹. The lower voltage cutoff upon discharge was 1.5 V. (b) EELS of Mn L-edge and (c) Raman spectra for LiF@MnO before charge, and after CC or CC-CV charge as indicated. (d) High-resolution Li 1s and Mn 3p XPS spectra of the pristine MnO electrode and LiF@MnO at different charge/discharge states. The XPS profile for pristine MnO, CC charged, CC-CV charged, and discharged electrodes are normalized by the Mn 3p peak integrated area. Binding energy reference peaks: LiF 55.7 eV, Mn₂O₃ 49.5 eV, Mn₃O₄ 49.1 eV, and MnO 48.1 eV.^[17] To avoid binder-induced fluoridation, PAN binder was used in the cathode instead of PVDF.

2.3 Rate capability of Mn-O-F derived from different fluorination sources

We next investigated the attainable rate performance of the first Mn-O-F discharge/lithiation (Figure 5a), with the derived Ragone plot and comparison with other MnO/LiF methodologies shown in Figure 5b. The MnO utilization (#e⁻/MnO) is calculated based on the discharge/lithiation capacity, with the calculation details described in the SI. The highest MnO utilization were achieved at low rate (<30 mA g_{MnO}⁻¹) in all systems. The LiF@MnO (~400 nm) exhibits high MnO utilization (~0.9 e⁻/MnO), comparable to the nano-scale (~8 nm) ball-milled MnO/LiF composites reported previously,^[9b] and much higher than that of ball-milled MnO/LiF with ~40 nm particle size (<0.7 e⁻/MnO). This indicates that the stringent particle size

limitation of MnO in previous studies is no longer critical when LiF is nano-crystallized and in intimate contact with MnO. In addition, the MnO/LiPF₆ system reported elsewhere, where LiF is formed *in situ* from LiPF₆ decomposition,^[11b] used MnO particles with size ~50 nm – 2 μm, similar to that of LiF@MnO, but only exhibits ~ 0.5 e⁻/MnO utilization at ~25 mA g_{MnO}⁻¹. As for the rate capability, LiF@MnO demonstrated the highest MnO utilization among all MnO/LiF systems with particle sizes ≥40 nm. Notably, a relatively steep capacity decrease, from 343 mAh g_{MnO}⁻¹ to 184 mAh g_{MnO}⁻¹, was observed for LiF@MnO as the current density increased from 20 mA g_{MnO}⁻¹ (~0.05 C) to 60 mA g_{MnO}⁻¹ (~0.15 C). Further increasing the current density to up to 150 mA g_{MnO}⁻¹ results in capacity drop to ~100 mAh g_{MnO}⁻¹. It is noted that, when cycled at low rates (≤ 20 mA g_{MnO}⁻¹), although the attainable capacities are similar, lowering the current density is helpful for reducing voltage hysteresis of LiF@MnO between charge and discharge (Figure 5a). A similar trend was also observed for ball-milled MnO/LiF prepared in this work, where the capacity decreased from 259 mAh g_{MnO}⁻¹ to 136 mAh g_{MnO}⁻¹ as the rate increased to ~60 mA g_{MnO}⁻¹, and was comparable to that of LiF@MnO at the highest current density of ~150 mA g_{MnO}⁻¹. Therefore, this suggests that the conversion reaction between Mn-O-F and MnO-LiF is kinetically limited, regardless of the LiF morphology, which may be caused by slow diffusion in the solid phase.

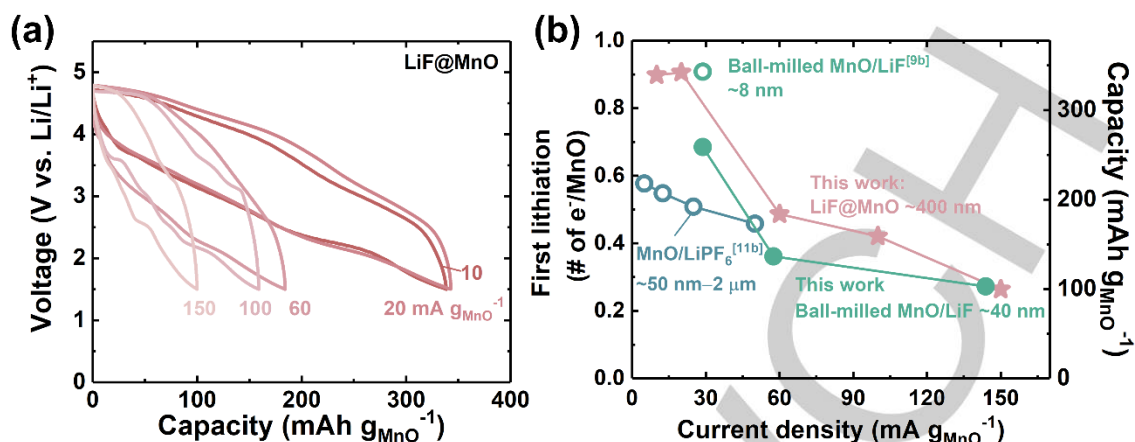


Figure 5. (a) Rate capability of Mn-O-F. The discharge rate of 10, 20, 60, 100, 150 mA g_{MnO}⁻¹ correspond to 0.025, 0.05, 0.15, 0.25, and 0.40 C, respectively. The Mn-O-F were derived from LiF@MnO (from fully discharged Li-SF₆ cells; also used for part b) by first CC charge at the corresponding rates to 4.8 V and then CV hold till current drop to half of the initial current. (b) Ragone plot comparing the electrochemical performance of LiF-MnO systems as Li-ion cathodes: Ball-milled MnO/LiF composite with an average particle size of ~8 nm (data from Ref.^[9b]) or ~40 ± 25 nm (synthesized and measured in this study); LiF formed *via* LiPF₆ decomposition (data from Ref.^[11b]); and electrochemically-formed LiF@MnO (this study).

2.4 Trace SF₆ as additive for improved cyclability

When cycled at 20 mA g_{MnO}⁻¹ (~0.05 C) with 1 M LiClO₄ EC/DMC electrolyte, both LiF@MnO and ball-milled MnO/LiF (~40 ± 25 nm) showed capacity fade from ~340 and 259 mAh g_{MnO}⁻¹ respectively to ~170 mAh g_{MnO}⁻¹ after 20 cycles (**Figure 6a**). The capacity fade can be attributed in part to the severe morphological changes upon repeated lithiation/delithiation and corresponding conversion of Mn-O-F to LiF-MnO, leading to gradual electronic disconnection and loss of active F for re-incorporation into the parent MnO phase.^[11a] Therefore, instead of fluorinated salts as used previously to resupply F to the MnO phase,^[11] we here demonstrate that regulated amounts of dissolved SF₆ (SF₆ solubility in organic solvents: ~ 2 mM)^[14a] can function as an effective electrolyte additive and F source. These experiments also allowed examination of the potential for LiF formation and cycling to occur in the same cell, *i.e.* avoiding the need to change electrolyte to remove residual gas as before. The initial high-capacity LiF formation step was therefore conducted first in a Li-SF₆ cell discharged to full capacity in 1

M LiClO₄ EC/DMC electrolyte (**Figure S8**). Following charge activation and direct cycling with an SF₆ gas headspace present, a long discharge plateau (~250 mAh g_{MnO}⁻¹) at ~2.5 V was observed upon subsequent discharge, the features of which are similar to that observed in Li-SF₆ cells with a characteristic “sudden death” (voltage drop) in the end of discharge (**Figure 5b**). These features indicate that the discharge activity upon cycling remains governed by SF₆ reduction when there is a large reservoir of SF₆ in the cell. The slightly increased SF₆ discharge potential at ~2.4 V (discharge potential of SF₆ cell at the same rate with pristine MnO/VC is ~2.0 V, **Figure S9**) is unclear at present, but could be attributed to a cathode morphology change caused by MnO fluoridation. Though good capacity retention (>270 mAh g_{MnO}⁻¹) was attained for the first five cycles, the cell discharge capacity dropped rapidly to ~180 mAh g_{MnO}⁻¹ by the 9th cycle and became unstable (exhibited significant voltage fluctuation) at the 14th cycle causing cell termination (**Figure 5c**). We hypothesize that the instability observed from extended cycling can be attributed to the accumulation of excessive LiF/F⁻ in the cathode, which is detrimental given passivating qualities of LiF.

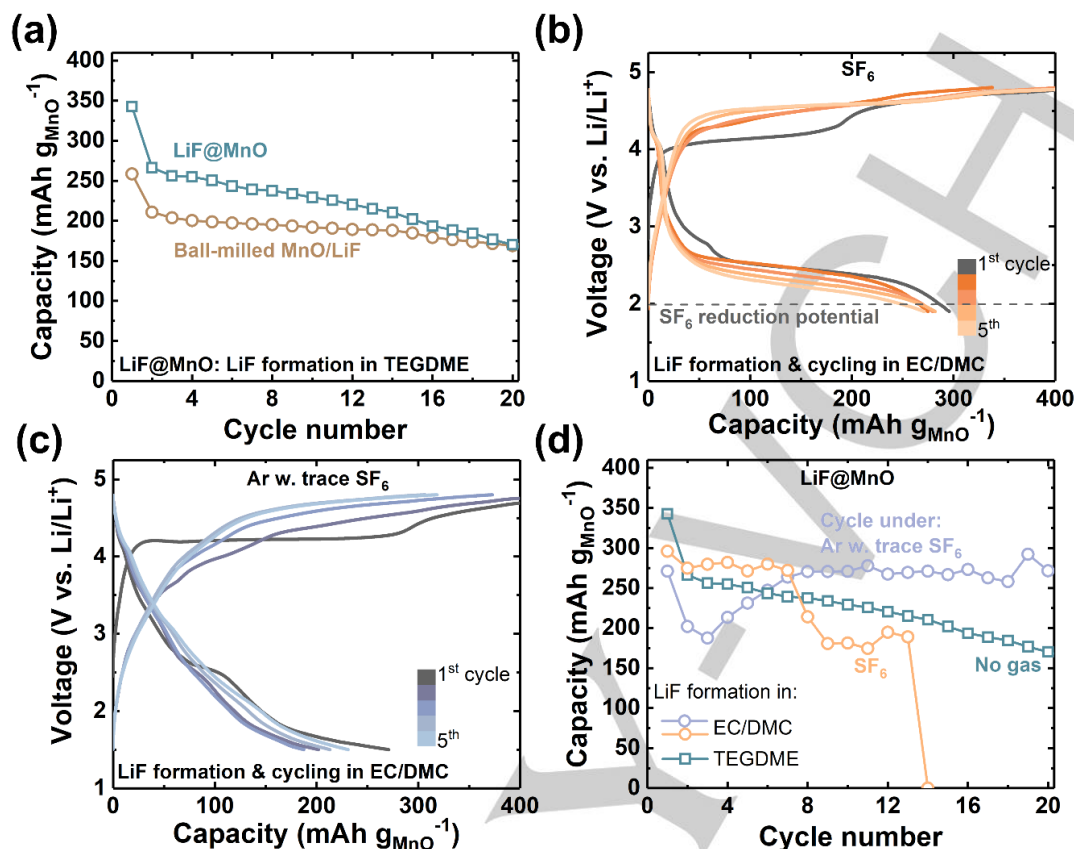


Figure 6. (a) Discharge capacities as a function of cycle number of ball-milled MnO/LiF (~40 nm) cathodes and LiF@MnO cathodes (LiF formed from SF₆ discharge in 0.1 M LiClO₄ TEGDME electrolyte). (b) and (c) Electrochemical profiles of the first five cycles of LiF@MnO (LiF formed from SF₆ reduction in 1 M LiClO₄ EC/DMC electrolyte). After LiF formation, (b) the cell was directly cycled under SF₆, or (c) purged with Ar, then cycled. (d) Discharge capacities as a function of cycle number of LiF@MnO cathodes in part (b) and (c), compared with the LiF@MnO with LiF formed in TEGDME electrolyte and cycled with no gas present (same data as LiF@MnO in part a). All cells were cycled with 1 M LiClO₄ in EC/DMC electrolyte at 20 mA g_{MnO}⁻¹ (~0.05 C).

To test this hypothesis and to further improve the cyclability, following the LiF-forming discharge step in 1 M LiClO₄ EC/DMC, cells were then briefly purged with Ar prior to continued cycling to remove excessive SF₆ in the headspace. A discharge profile similar to that of LiF@MnO without SF₆ (Figure 3c) is obtained, with the exception of a slightly extended tail at the end of discharge at ~1.5 V (Figure 5c). This is likely caused by the trace amount of SF₆ left in the cell that was not removed by Ar purging due to the high molecular weight of SF₆. The lower SF₆ reduction voltage than that observed with extra SF₆

present (Figure 5b) can be attributed to the concentration overpotential. Despite the lower capacity ($271 \text{ mAh g}_{\text{MnO}}^{-1}$ vs. $340 \text{ mAh g}_{\text{MnO}}^{-1}$ for LiF@MnO formed with TEGDME electrolyte) at the beginning of cycling, which might be caused by the solvent-induced LiF crystallinity and particle size difference, this cell exhibits an improved cyclability with capacity higher than $270 \text{ mAh g}_{\text{MnO}}^{-1}$ retained after 20 cycles (Figure 5c). The detailed mechanism of continued SF_6 reactivity over cycling will be investigated in future studies. However, these findings overall indicate the potential to explore future electroactive F additives to dynamically repair oxide phases as they become F-depleted. In particular, reduction of perfluorinated gases as studied herein occurs well within the electrochemical stability window of the electrolyte, providing a potentially softer fluorination route than those currently reported. The overall fluorination methodology is, however, currently limited by aggressive high voltages and charge protocols demanded by the intrinsic oxide redox states, which are too high for MnO to likely be feasible for practical cells. We anticipate potential for this methodology of LiF coating and dynamic fluoridation to be adaptable to future oxide substrates with lower oxidation potentials and more complex structures beyond that of the simpler binary phases.

3. Conclusions

Activation of the binary oxide MnO to MnOF in the presence of LiF was demonstrated using electrochemically-formed LiF grown by the reduction of perfluorinated gas. The small feature size of LiF, which grows directly onto the electronically conductive surfaces of MnO and is therefore in intimate contact with the substrate, allows for effective LiF splitting upon subsequent charge and a high degree of fluoridation, as indicated by high capacities (up to 340 mAh g^{-1}) subsequently accessible upon Li^+ cycling. These capacities correspond to high MnO utilization ($\sim 0.9 \text{ e}^-/\text{MnO}$) and are obtained with moderate particle sizes ($\sim 400 \text{ nm}$), demonstrating that the stringent particle size requirement for high MnO utilization observed in previous studies ($<10 \text{ nm}$) is not necessary as long as LiF is nano-crystallized and in intimate contact with

MnO. The LiF@MnO exhibits improved rate capability compared to other methodologies used to source LiF into a MnO cathode with particle sizes ≥ 40 nm. Additionally, SF₆ was shown to be an effective electrolyte additive to support an F-enriched environment near MnO during cycling, leading to stable cycling with capacities ~ 270 mAh g_{MnO}⁻¹ at 20 mA g_{MnO}⁻¹ over at least 20 cycles. This study indicates that previously-reported limits on oxide fluoridation can be overcome by methodologies that allow for improved control over LiF quantity, particle sizes, and overall morphology, which can further contribute to the development of other high-performance cell cathode materials with F substitution (*e.g.* Li-containing oxides with disordered rock-salt or layered structures) in future work.

Experimental Section

Chemicals and Materials: All chemicals, electrodes and cell-making materials were thoroughly dried and stored in an argon-filled glovebox (H₂O content <0.3 ppm, O₂ content <0.3 ppm, MBRAUN). LiClO₄ (99.99% trace metals basis, Sigma-Aldrich) and the Whatman filter paper (Grade QM-A, 2.2 μ m pore size, 450 μ m in thickness, Sigma Aldrich) were dried under active vacuum for 24 hours at 120 °C in a Buchi glass oven. TEGDME (99%, Sigma-Aldrich), propylene carbonate (PC, 99.7%, Sigma-Aldrich), EC (99%, Sigma-Aldrich), DMC (> 99.9%, Sigma-Aldrich), and MnO (99%, Sigma-Aldrich) were stored inside the glovebox at room temperature.

Cathode Preparation: The as-received MnO particles (~ 0.25 mm) were combined with Vulcan carbon (VC) (XC-72, Cabot Corporation) (MnO:VC=7:2 w/w), sealed in the glovebox, and ball-milled by a SPEX ball mill for 3 h. The ball-milled MnO/LiF composites were prepared by mixing the MnO with LiF (MnO:LiF = 1:1.2 m/m), as well as VC (20 wt% of total MnO/LiF composite) for 48 h using planetary milling at 400 r.p.m. (Retsch GmbH, Germany). The MnO/VC, and ball-milled MnO/LiF cathodes were fabricated in-house

by uniformly coating sonicated inks composed of the as-prepared MnO composites, additional VC, N-Methyl-2-pyrrolidone (NMP), and polyvinylidene difluoride (PVDF) (with a weight ratio of PVDF:VC:MnO = 10:20:70) onto a sheet of Toray paper (TGP-H-030, Fuel cell earth). The final weight ratio of PVDF:VC:MnO = 10:35:55. The obtained coated Toray paper was dried at room temperature prior to being punched into circular disks (12 mm diameter), with a typical MnO loading of $1.12 \pm 0.17 \text{ mg}_{\text{MnO}} \text{ cm}^{-2}$ (error bar represents five measurements). The MnO cathodes were subsequently dried under active vacuum in a glass oven (Buchi) overnight at 90 °C.

Galvanostatic Discharge for LiF Formation: Two-electrode Swagelok-type Li-perfluorinated gas cells were constructed in an argon glovebox, with MnO cathode and a 9 mm diameter disk of Li metal as anode (0.75 mm thick, 99.9% metals basis, Alfa Aesar), which was prestabilized by soaking in 0.1 M LiClO₄ in PC for more than three days before use.^[24] The separator (13 mm diameter glass fiber filter paper) was impregnated with 150 µL electrolyte solution (0.1 M LiClO₄ in TEGDME). SF₆ (Airgas, 99.999% purity) or NF₃ (Airgas, 99.999% purity) gas was introduced into cells following their assembly by purging the gas into the cell headspace within the glovebox for approximately 3 min, pressurizing it to ~1.6 bar, and then sealing the cell that contains excess amounts of SF₆ or NF₃ gas for subsequent discharge outside the glovebox. The cells were rested at open circuit voltage (OCV) for 15 h before the galvanostatic discharge process, which were carried out (BioLogic VMP3 potentiostat or MPG2 workstation) at the specified current density with a voltage window ranging from OCV to a lower cutoff voltage of 1.6 V vs Li/Li⁺. The discharged cathodes were extracted from the cell, rinsed with dimethoxyethane (DME), dried and stored inside the glovebox.

Electrochemical Characterization: Two-electrode Swagelok-type Li-ion cells were constructed and sealed in an argon glovebox, with the Li metal as the anode and the LiF-coated or pristine MnO electrode (as indicated) as the cathode. The cells were cycled on a BioLogic VMP3 with 150 µL 1 M LiClO₄ in EC/DMC

(1:1 v/v) electrolyte impregnated into a glass fiber separator. Unless otherwise indicated, the cells were first constant current (CC) charged to 4.8 V, then constant voltage (CV) charged until the current dropped to half of the current used for CC charge. After the first charge process, the cells were galvanostatically cycled at the same rate as that for the first CC charge between 1.5 and 4.8 V.

Scanning Electron Microscopy (SEM): After charge/discharge, the cell was disassembled inside the glovebox and the cathode was extracted, rinsed with DME, and dried in the argon glovebox prior to SEM characterization. The sample, which was sealed in a glass vial in the glovebox, was then quickly transferred into the SEM chamber for the measurement to minimize the exposure to ambient. All the SEM characterizations were conducted on a Zeiss Merlin High-resolution SEM operating at an accelerating voltage of 5 kV and beam current of 100 pA.

X-ray Diffraction (XRD): Both pristine and tested/rinsed discharged cathodes were stored inside the glovebox. Prior to XRD measurements, the samples were sealed in an air-sensitive sample holder in the glovebox to minimize atmospheric contamination. XRD patterns were collected on a PANalytical X'Pert Pro multipurpose diffractometer with a copper anode (Cu K α). All scans for cathode characterization were performed from $5^\circ < 2\theta < 90^\circ$ at a typical scan speed of $0.5^\circ \text{ min}^{-1}$. Reference data for LiF: space group: Fm $\bar{3}$ m, JCPDS: 00-004-0857.

Spectroscopic Measurements: ^{19}F Nuclear Magnetic Resonance (NMR) measurements were performed using a Bruker Advance Neo 400 MHz NMR spectrometer. Samples were dissolved in deuterated D_2O (Sigma-Aldrich) with 2,2,2-trifluoroethanol (TFE, Sigma-Aldrich) as an internal reference. The solutions were then transferred into capped NMR tubes (Wilmad, 528-PP-7) for NMR analysis. Raman spectroscopy was performed on the rinsed charged/discharged cathodes using Renishaw Invia Reflex Micro Raman instrument

with a laser excitation wavelength of 785 nm. X-ray photoelectron spectroscopy (XPS) analysis was conducted on a PHI VersaProbe II X-ray Photoelectron Spectrometer. The binding energies were calibrated by the adventitious carbon peak at 284.80 eV. Electron energy loss spectroscopy (EELS) was carried out on a JEOL 2010 FEG analytical electron microscope equipped with a Gatan image filter for EELS, operating at 200 kV in the parallel beam mode. The samples were quickly transferred into the TEM chamber for the measurement with minimum exposure to ambient.

Supporting Information

Supporting Information is available from the Wiley Online Library or from the author.

Acknowledgements

The authors gratefully acknowledge funding from the Army Research Office under award number W911NF-19-1-0311 and from the MIT Energy Initiative Energy Storage Center. This work made use of the MRSEC Shared Experimental Facilities at MIT, supported by the National Science Foundation under award number DMR-14-19807.

Conflict of Interest

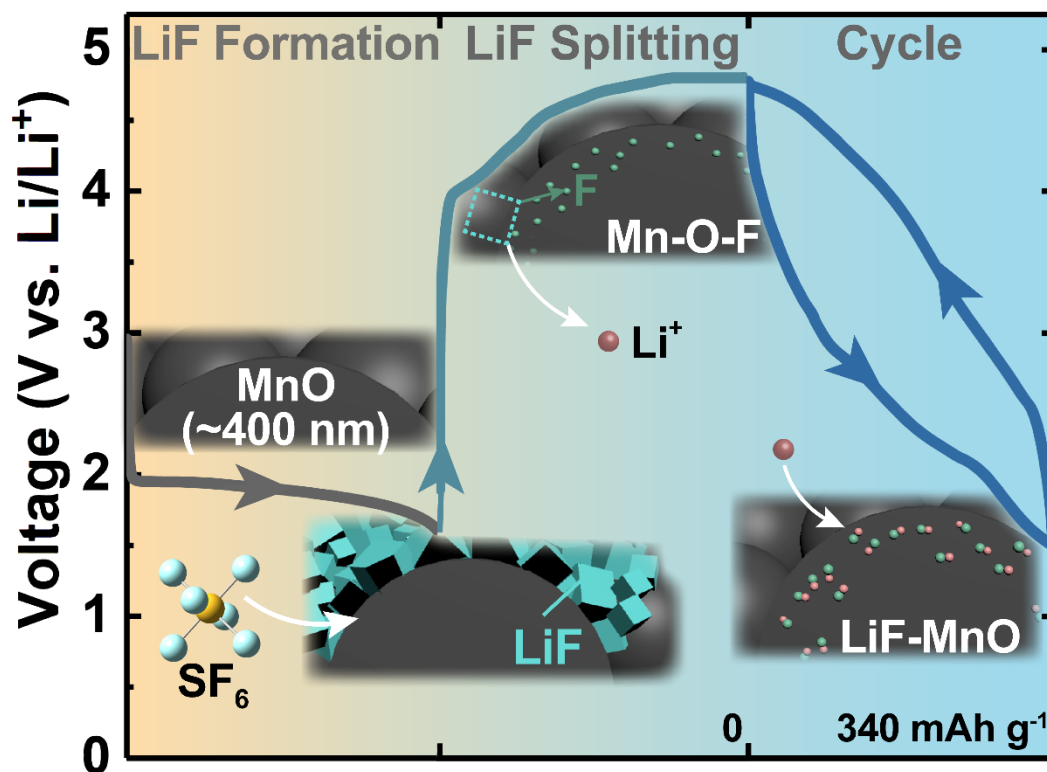
The authors declare no conflict of interest.

Keywords: Electrochemistry, Energy conversion, Fluorides

References

- [1] a) K. Kang, Y. S. Meng, J. Bréger, C. P. Grey, G. Ceder, *Science* **2006**, 311, 977; b) M. Armand, J. M. Tarascon, *Nature* **2001**, 414, 359.
- [2] R. Schmich, R. Wagner, G. Hörpel, T. Placke, M. Winter, *Nat. Energy* **2018**, 3, 267.
- [3] P. Rozier, J. M. Tarascon, *J. Electrochem. Soc.* **2015**, 162, A2490.
- [4] R. Clément, Z. Lun, G. Ceder, *Energy Environ. Sci.* **2020**, 13, 345.
- [5] a) K. S. Lee, S. T. Myung, K. Amine, H. Yashiro, Y. K. Sun, *J. Electrochem. Soc.* **2007**, 154, A971; b) J. Yang, L. Xiao, W. He, J. Fan, Z. Chen, X. Ai, H. Yang, Y. Cao, *ACS Appl. Mater. Interfaces* **2016**, 8, 18867; c) D. H. Seo, J. Lee, A. Urban, R. Malik, S. Kang, G. Ceder, *Nat. Chem.* **2016**, 8, 692.
- [6] a) A. Windmüller, C.-L. Tsai, S. Möller, M. Balski, Y. J. Sohn, S. Uhlenbruck, O. Guillon, *J. Power Sources* **2017**, 341, 122; b) Y. Wang, H. T. Gu, J. H. Song, Z. H. Feng, X. B. Zhou, Y. N. Zhou, K. Wang, J. Y. Xie, *J. Phys. Chem. C* **2018**, 122, 27836; c) S.-H. Kang, K. Amine, *J. Power Sources* **2005**, 146, 654; d) J. Lee, D. A. Kitchaev, D. H. Kwon, C. W. Lee, J. K. Papp, Y. S. Liu, Z. Lun, R. J. Clément, T. Shi, B. D. McCloskey, J. Guo, M. Balasubramanian, G. Ceder, *Nature* **2018**, 556, 185; e)

- P. Yue, Z. Wang, J. Wang, H. Guo, X. Xiong, X. Li, *Powder Technol.* **2013**, 237, 623; f) J. K. Ko, K. M. Wiaderek, N. Pereira, T. L. Kinnibrugh, J. R. Kim, P. J. Chupas, K. W. Chapman, G. G. Amatucci, *ACS Appl. Mater. Interfaces* **2014**, 6, 10858; g) X. Xiong, Z. Wang, X. Yin, H. Guo, X. J. M. L. Li, *Mater. Lett.* **2013**, 110, 4.
- [7] G. G. Amatucci, N. Pereira, *J. Fluorine Chem.* **2007**, 128, 243.
- [8] A. Windmüller, C.-L. Tsai, S. Möller, M. Balski, Y. J. Sohn, S. Uhlenbruck, O. Guillon, *J. Power Sources* **2017**, 341, 122.
- [9] a) N. Dimov, A. Kitajou, H. Hori, E. Kobayashi, S. Okada, *ECS Trans.* **2014**, 58, 87; b) S. K. Jung, H. Kim, M. G. Cho, S. P. Cho, B. Lee, H. Kim, Y. U. Park, J. Hong, K. Y. Park, G. Yoon, Won M. Seong, Y. Cho, Myoung H. Oh, H. Kim, H. Gwon, I. Hwang, T. Hyeon, W. S. Yoon, K. Kang, *Nat. Energy* **2017**, 2, 16208; c) S.-K. Jung, I. Hwang, S.-P. Cho, K. Oh, K. Ku, I. R. Choi, K. Kang, *Chem. Mater.* **2018**, 30, 1956.
- [10] S. K. Jung, I. Hwang, I. R. Choi, G. Yoon, J. H. Park, K. Y. Park, K. Kang, *Adv. Energy Mater.* **2019**, 9, 1900503.
- [11] a) L. Zhang, G. Chen, E. J. Berg, J. M. Tarascon, *Adv. Energy Mater.* **2017**, 7, 1602200; b) L. Zhang, D. Dambournet, A. Iadecola, D. Batuk, O. J. Borkiewicz, K. M. Wiaderek, E. Salager, M. Shao, G. Chen, J. M. Tarascon, *Chem. Mater.* **2018**, 30, 5362.
- [12] a) Y. Zhao, K. Wei, H. Wu, S. Ma, J. Li, Y. Cui, Z. Dong, Y. Cui, C. Li, *ACS Nano* **2019**, 13, 2490; b) K. Wei, Y. Zhao, K. Chen, K. Sun, T. Wu, Z. Dong, Y. Cui, C. Zeng, C. Li, *Adv. Funct. Mater.* **2021**, 2009133.
- [13] F. Jiang, P. Peng, *Sci. Rep.* **2016**, 6, 1.
- [14] a) Y. Li, A. Khurram, B. M. Gallant, *J. Phys. Chem. C* **2018**, 122, 7128; b) H. Gao, Y. Li, R. Guo, B. M. Gallant, *Adv. Energy Mater.* **2019**, 1900393.
- [15] M. He, Y. Li, R. Guo, B. M. Gallant, *J. Phys. Chem. Lett.* **2018**, 9, 4700.
- [16] P. Poizot, S. Laruelle, S. Grugeon, L. Dupont, J. Tarascon, *Nature* **2000**, 407, 496.
- [17] *The NIST x-ray photoelectron spectroscopy database*, National Institute of Standards and Technology, Gaithersburg MD **2000**.
- [18] SDBSWeb, National Institute of Advanced Industrial Science and Technology.
- [19] a) M. M. Ottakam Thotiyl, S. A. Freunberger, Z. Peng, P. G. Bruce, *J. Am. Chem. Soc.* **2012**, 135, 494; b) R. Imhof, P. Novák, *J. Electrochem. Soc.* **1999**, 146, 1702.
- [20] S. Bernardini, F. Bellatreccia, A. Casanova Municchia, G. Della Ventura, A. Sodo, *J. Raman Spectrosc.* **2019**, 50, 873.
- [21] a) Y. Mai, D. Zhang, Y. Qiao, C. Gu, X. Wang, J. Tu, *J. Power Sources* **2012**, 216, 201; b) I. Rusakova, T. Ould-Ely, C. Hofmann, D. Prieto-Centurión, C. S. Levin, N. J. Halas, A. Lüttge, K. H. Whitmire, *Chem. Mater.* **2007**, 19, 1369; c) X. Li, Y. Zhu, X. Zhang, J. Liang, Y. Qian, *RSC Adv.* **2013**, 3, 10001.
- [22] D. T. Zahn, *Phys. Chem. Chem. Phys.* **1999**, 1, 185.
- [23] C. Julien, M. Massot, C. Poinsignon, *Spectrochim. Acta A* **2004**, 60, 689.
- [24] Z. Peng, S. A. Freunberger, Y. Chen, P. G. Bruce, *Science* **2012**, 337, 563.



Conformal LiF coating of MnO cathodes are achieved electrochemically by perfluorinated-gas reduction. The LiF-modified MnO is then activated upon charge to form an Mn-O-F conversion Li-ion cathode. This methodology allows nano-crystallized LiF to grow in intimate contact with MnO, resulting in high MnO utilization (~ 0.9 e⁻/MnO) with large MnO particle size (~ 400 nm), exceeding MnO/LiF systems reported to date.

Supporting Information

Electrochemical Fluoridation of Manganese Oxide by Perfluorinated-Gas Conversion for Li-ion Cathodes*Haining Gao, Mingfu He, Rui Guo and Betar M. Gallant****Calculation of MnO utilization ($\#e^-/\text{MnO}$)**

The $\#e^-/\text{MnO}$ was calculated based on the discharge capacity Q ($\text{mAh g}_{\text{MnO}}^{-1}$), following the equation below:

$$\#e^-/\text{MnO} = \frac{Q}{F / 3.6 / \text{MW}_{\text{MnO}}} ,$$

Where F is Faraday constant (96485 C mol^{-1}), and MW_{MnO} is the molar mass of MnO (70.9 g mol^{-1}).

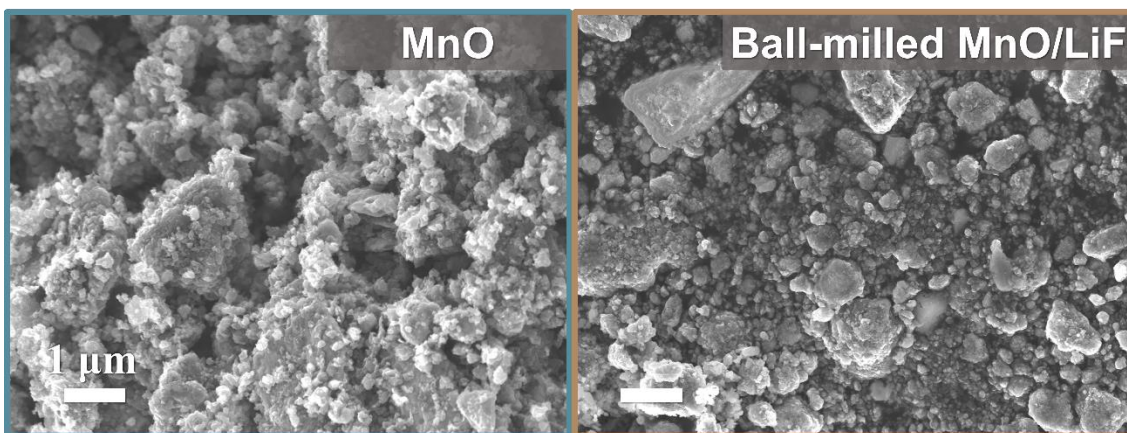


Figure S1. SEM of the ball-milled MnO and MnO/LiF powders (as indicated). Due to the large particle size of the as-received MnO ($\sim 0.25 \text{ mm}$), a short ball-mill of 3 h was conducted on MnO/Vulcan carbon (VC) mixture (MnO:VC=7:2 w/w) to reduce the particle size. The MnO/LiF composite (MnO:LiF = 1:1.2 m/m) contains 20 wt% of VC and was ball-milled for 48 h.

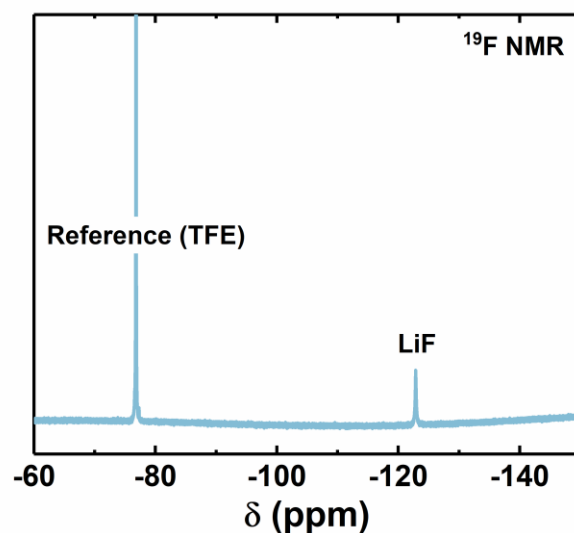


Figure S2. ^{19}F Nuclear Magnetic Resonance (NMR) spectra of the discharged MnO cathode (under SF_6) after soaking in D_2O . 2,2,2-trifluoroethanol was added into the solvent as reference.

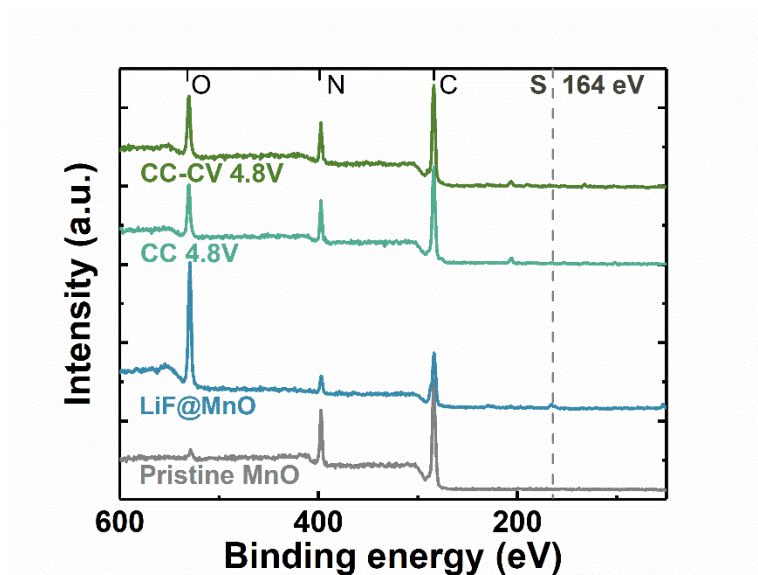


Figure S3. XPS survey scans of a pristine MnO/VC electrode, of LiF@MnO before first charge, and of LiF@MnO after first charge (LiF splitting) following either a constant current (CC) or constant current-constant voltage (CC-CV) protocol.

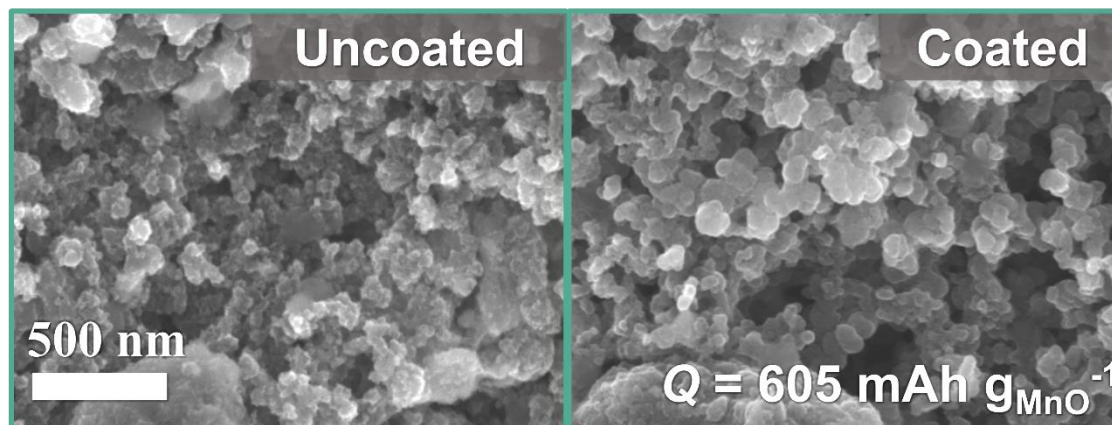


Figure S4. SEM of MnO/VC cathodes in partially discharged Li-SF₆ cell, with a capacity of ~605 mAh g_{MnO}⁻¹ (corresponding to LiF amount of 454 mAh g_{MnO}⁻¹). Two different morphologies were observed: the one on the left shows small discrete particles, which is the pristine (uncoated) morphology; while the one on the right shows larger particle sizes with film-like structure, indicating the presence of the coating layer.

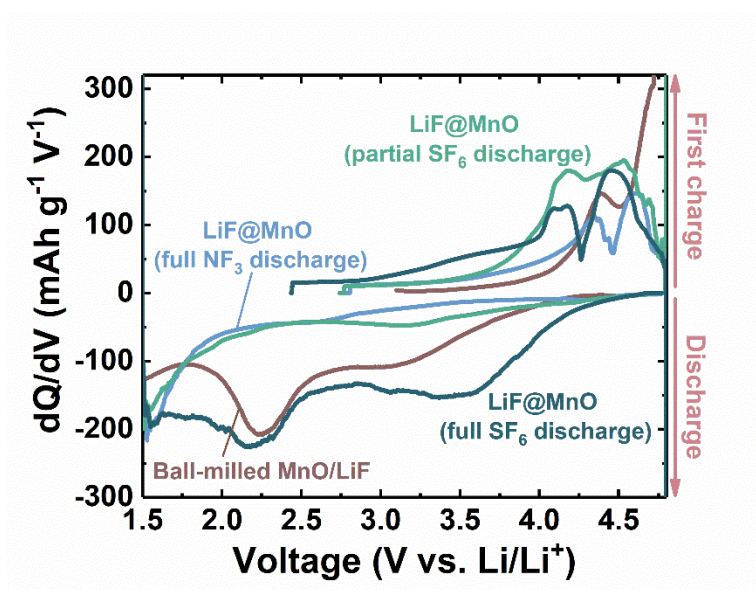


Figure S5. Differential capacity plot derived from the galvanostatic discharge profiles in Figure 3.

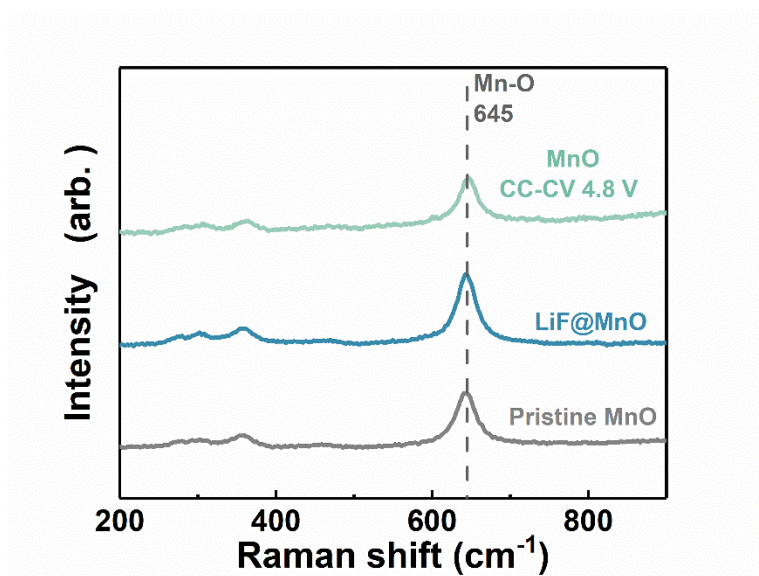


Figure S6. Raman spectra of the pristine MnO/VC electrode, LiF@MnO (uncharged), and CC-CV charged MnO/VC (without LiF presence). Negligible change in Mn bonding environment can be observed.

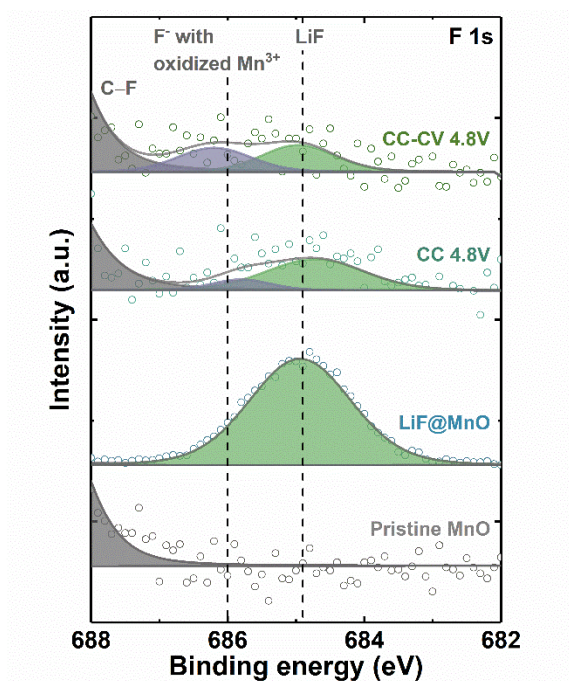


Figure S7. High-resolution F 1s XPS spectra of the pristine MnO electrode and LiF@MnO at different charge states. Binding energy reference peaks: LiF 684.9 eV, covalent C-F 689.4 eV,^[1] and F⁻ with oxidized Mn³⁺ 686.0 eV.^[2] To avoid binder-induced fluoridation, PAN binder was used in the cathode instead of PVDF. The covalent C-F signal were from substrate Toray paper. Due to the weaker adhesion of PAN, some electrode powder was detached from the substrate after long cell testing and the underlying Toray paper became exposed, resulting in strong C-F signal. As a result, the ionic F signal is relatively weak.

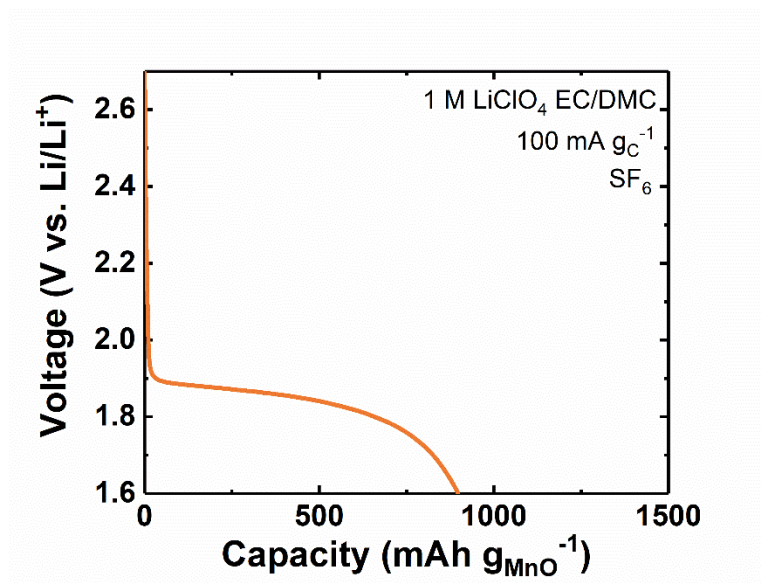


Figure S8. Galvanostatic discharge profile of Li-SF₆ cell with MnO/VC as cathode substrate and 1 M LiClO₄ EC/DMC as electrolyte at a rate of 100 mA g_C⁻¹.

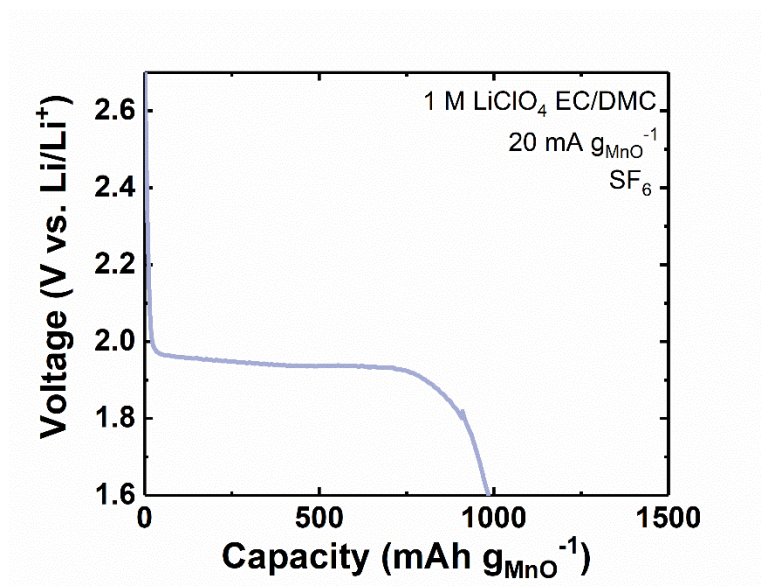


Figure S9. Galvanostatic discharge profile of Li-SF₆ cell with MnO/VC as cathode substrate and 1 M LiClO₄ EC/DMC as electrolyte at a rate of 20 mA g_{MnO}⁻¹.

References

- [1] *The NIST x-ray photoelectron spectroscopy database*, National Institute of Standards and Technology, Gaithersburg MD **2000**.
- [2] S. K. Jung, H. Kim, M. G. Cho, S. P. Cho, B. Lee, H. Kim, Y. U. Park, J. Hong, K. Y. Park, G. Yoon, Won M. Seong, Y. Cho, Myoung H. Oh, H. Kim, H. Gwon, I. Hwang, T. Hyeon, W. S. Yoon, K. Kang, *Nat. Energy* **2017**, 2, 16208.